Supplementary Materials for

Crosstalk Between Microtubule Attachment Complexes Ensures Accurate Chromosome Segregation

Dhanya K. Cheerambathur, Reto Gassmann, Brian Cook, Karen Oegema, & Arshad Desai*

Correspondence to: abdesai@ucsd.edu

This PDF file includes:

Materials & Methods:

C. elegans strains & methods

C. elegans strains used in this study are listed in Table S1. Strains carrying integrated single-copy RNAi-resistant *spdl-1* and *ndc-80* transgenes were constructed using the MosSCI method as previously described (*28*). Transgene integration was confirmed by PCR of regions spanning each side of the insertion.

Genetic analysis was performed using the *ndc-80(tm5271)* deletion which causes 100% larval lethality when homozygous. Strains heterozygous for *ndc-80(tm5271)* (on Chr IV) and homozygous for a specific *ndc-80* transgene (inserted on Chr II) were generated by standard genetic methods. Approximately 200 F1 progeny (L4 stage) from each strain were singled and placed for 48 hrs at 20°C. Each plate was scored for visible phenotype(s) of the F1 worm as well as for presence of embryos, and the F1 worm (which on certain plates was an arrested larvae or a highly abnormal sterile adult) was then removed and genotyped to identify those that were homozygous for the *ndc-80(tm5271)* deletion. When applicable, the fate of embryos laid by worms homozygous for a *ndc-80* transgene and *ndc-80(tm5271)* deletion was scored 2 days later; plates homozygous for *ndc-80(tm5271)* with viable F2 progeny that could be propagated through multiple generations enabled establishment of stably rescued lines (such lines were never obtained for *ndc-80*$^{\Delta Tail}$ but were obtained for the other transgenes).

RNA-mediated Interference

All RNAi was performed by microinjection. Double-stranded RNAs were generated as described (*10*) using DNA templates prepared by PCR-amplifying regions using the oligonucleotides and templates in Table S2. L4 hermaphrodites were injected with dsRNA

and incubated at 20°C for 36–46 h before dissection and imaging of their embryos. For double depletions, dsRNAs were mixed to obtain an equal concentration of 1 mg/mL for each dsRNA. For lethality assays investigating the functionality of *spdl-1* and *ndc-80* transgenes, L4 worms injected with dsRNA were singled 24 hours post-injection. Adult worms were removed from the plates 48 hours post-injection and hatched larvae and unhatched embryos were counted 20 hours later at 20°C.

Immunoblotting

Immunoblots were performed on whole-worm extracts (15 worms per lane for 100% loading) with affinity purified antibodies to NDC-80 (*11*) and SPDL-1 (*7*) using anti–α-tubulin as a loading control (DM1-α; Sigma-Aldrich). The primary antibodies, rabbit anti-NDC-80 and rabbit anti-SPDL-1, were pre-incubated with 0.5 mL of immobilized *E.coli* lysate (Thermo Scientific) per µg of antibody at room temperature for 1hr before addition to the nitrocellulose membrane.

Yeast Two-Hybrid Analysis

Two-hybrid analysis was performed according to the manufacturer's instructions (MATCH-MAKER^{TM}, Clontech).

Live Imaging

For embryos expressing GFP:H2b and GFP:γ-tubulin, 5 x 2 µm z-stacks were collected with 2x2 binning and a 60x 1.4 NA PlanApo objective (Olympus) every 10 s at 19°C on a DeltaVision microscope (Applied Precision) equipped with a CoolSnap camera (Roper Scientific). Spindle pole separation was quantified as described (*11*). Imaging for all other worms strains was performed on an inverted Zeiss Axio Observer Z1 system with a

Yokogawa spinning-disk confocal head (CSU-X1), a 63x 1.4 NA Plan Apochromat objective, and a QuantEM: 512SC EMCCD camera (Photometrics).

Protein Expression & Purification

Open reading frames encoding all 4 subunits of the *C.elegans* NDC-80 complex were PCR-amplified from cDNA and cloned into polycistronic expression construct pST39 (*29*). Mutant versions were generated with the QuikChange Lightning Kit (Agilent Technologies). For expression of $R^{N}Z$, ROD-1^{1-418} and Zwl-1-6XHis were PCR amplified and cloned into pET21a and pACYCDuet-1 (Novagen), respectively. Proteins were expressed in BL21(DE3) cells at 20 °C for 3-4hrs. Induced BL21(DE3) cells were lysed in Lysis Buffer (50mM HEPES [pH 7.4], 300mM NaCl, 10mM imidazole, 5mM β-mercaptoethanol [BME]) and clarified at 42,000g for 30 min at 4°C. For NDC-80 complex purifications, the clarified extract was fractionated by 30% ammonium sulfate precipitation and the pellet resuspended in Lysis Buffer with 100mM NaCl. Ni-NTA agarose (Qiagen) was incubated with clarified lysates or resuspended ammonium sulfate pellets for 45min, washed with Wash Buffer (25mM HEPES [pH 7.4], 400mM NaCl, 10mM imidazole, 5mM BME), and eluted with 25mM HEPES [pH 7.4], 250mM NaCl, 250mM imidazole, 5mM BME. The eluted protein was desalted into 25mM HEPES [pH 7.4], 50mM NaCl, 1mM EDTA, 1mM BME with a EconoPac PD10 desalting column (Bio-Rad), loaded on an ion exchange column (NDC-80 WT & CH* on HiTrap SP HP, GE Healthcare & $R^{N}Z$ & NDC-80 ΔTail on Mono Q, GE Healthcare), and eluted with a linear salt gradient. The peak fractions from ion exchange were fractionated on a Superose 6 gel filtration column. Protein concentrations were determined using densitometry of Coomassie-stained gels relative to a BSA standard.

Microtubule Cosedimentation Analysis

Increasing amounts of taxol-stabilized microtubules were incubated with 100nM NDC-80 complex variants or 100 nM NDC-80 complex preincubated with R^NZ (10 min at room temperature) in 12.5mM HEPES [pH7.4], 5μM BSA and 50 mM (2 μM R^NZ) or 100mM (14 μM R^NZ) NaCl. Reactions were pelleted through a BRB80 + 40% glycerol cushion at 80,000 rpm in a TLA100 rotor at 25°C. An aliquot from the top was removed as the supernatant sample; the rest of the supernatant was discarded. The pellet was resuspended in BRB80 + 10mM $CaCl_2$ for 10 min on ice. Equivalent amounts of supernatant (S) and pellet (P) were analyzed by anti-NDC-80 immunoblotting.

In vitro Translation

$^{[35]}S$ labeled fragments of NDC-80 were prepared using TnT® Quick Coupled Transcription/Translation System (Promega). 10 μl of the in vitro translation lysate was incubated for 1hr at 4°C with 10 μg R^NZ complex (in 25mM HEPES [pH7.4], 100mM Nacl, 0.1% NP40, 10mM Imidazole) in a final volume of 50 μl, mixed with 30 μl of a 1:1 nickel agarose slurry equilibrated with the binding buffer for an additional hour at 4°C. Beads were washed three times with binding buffer, eluted using sample buffer and the elution analyzed by SDS-PAGE and autoradiography.

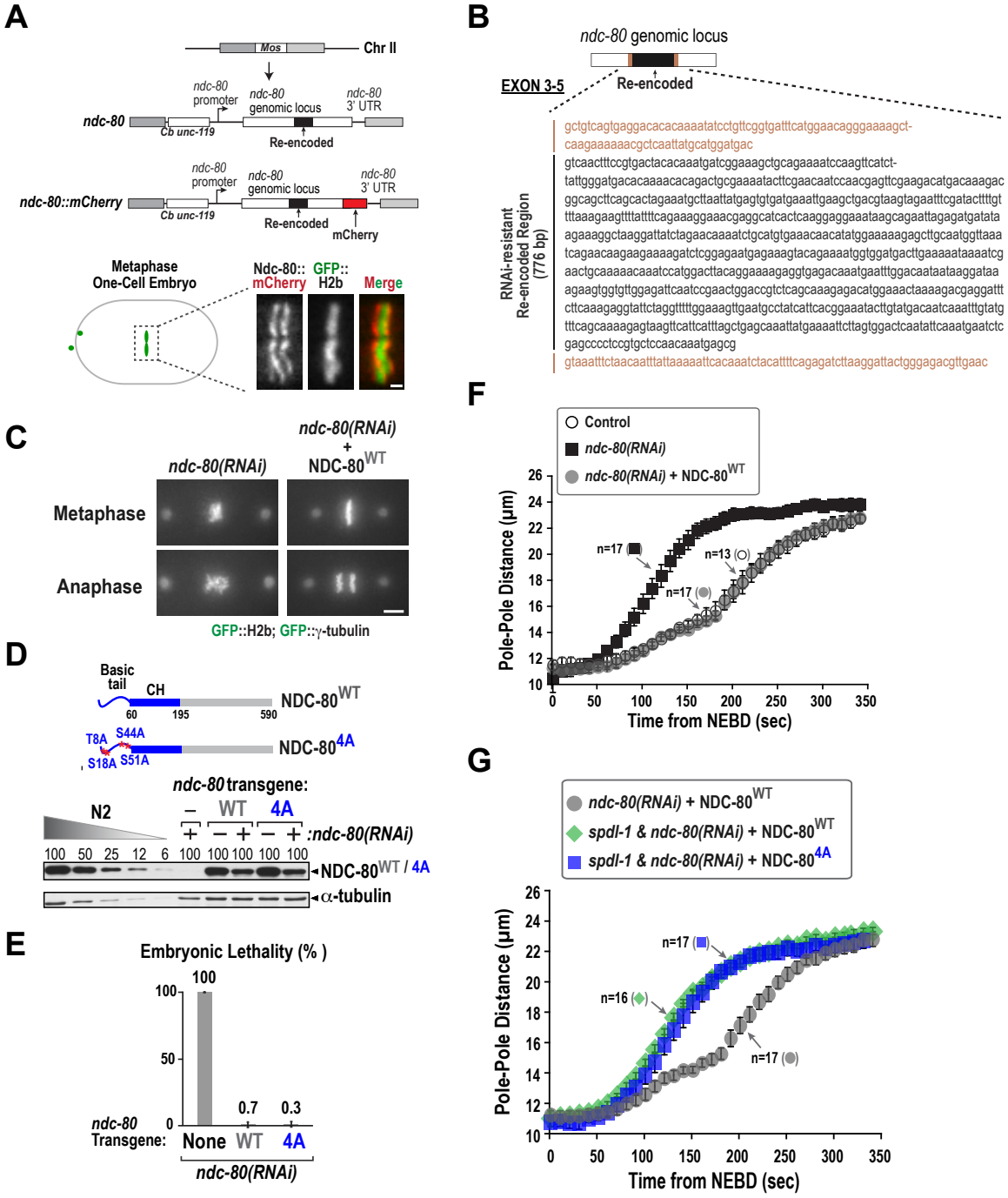

Fig. S1. An RNAi resistance-based replacement system for NDC-80 in the *C. elegans* embryo.

(A) Schematic of the RNAi-resistant *ndc-80* and *ndc-80::mCherry* transgene integrations (the single Mos transposon used for both integrations was located on Chromosome II). The *ndc-80::mCherry* transgene did not rescue depletion of endogenous NDC-80 as robustly as the untagged *ndc-80* transgene; hence, untagged *ndc-80* transgenes were used for all functional analysis. Images below show kinetochore localization of NDC-80::mCherry in metaphase one-cell stage embryos. Bar, 1 μm.

(B) Re-encoded nucleotide sequence of exons 3-5 of *ndc-80* that was used to generate the RNAi-resistant *ndc-80* transgene. A dsRNA corresponding to this region was used to deplete endogenous NDC-80 in all RNAi-based replacement experiments.

(C) Panels showing rescue of the chromosome alignment and segregation defects by the NDC-80^{WT} transgene following NDC-80 depletion. Bar, 5 μm.

(D) (*top*) Schematic of wild-type (WT) and Aurora B phosphosite mutant (4A) NDC-80. (bottom) Anti-NDC-80 immunoblot showing replacement of endogenous NDC-80 by transgene-encoded NDC-80 variants. α-tubulin serves as a loading control.

(E) Embryo viability analysis. Error bars are SD of embryo lethality per worm. >10 worms and >1000 embryos were scored per condition. Both the NDC-80^{WT} and the NDC-80^{4A} mutant rescue the embryonic lethality associated with endogenous NDC-80 depletion.

(F) & (G) Plot of spindle pole separation kinetics for the indicated conditions. Error bars represent the SEM with a 95% confidence interval. The plot in (*F*) demonstrates that NDC-80^{WT} (*gray circles*) perfectly rescues the premature pole separation defect observed following NDC-80 depletion (*black squares*). The control and *ndc-80(RNAi)* curves are the same as in *Fig. 1C*. The plot in (*G*) demonstrates that NDC-80^{WT} (green diamonds) and NDC-80^{4A} (*blue squares*) are equally sensitive to inhibition by RZZ (induced by depletion of SPDL-1). The control curve (*ndc-80(RNAi)* + NDC-80^{WT}) is the same as in *Fig. S1F*.

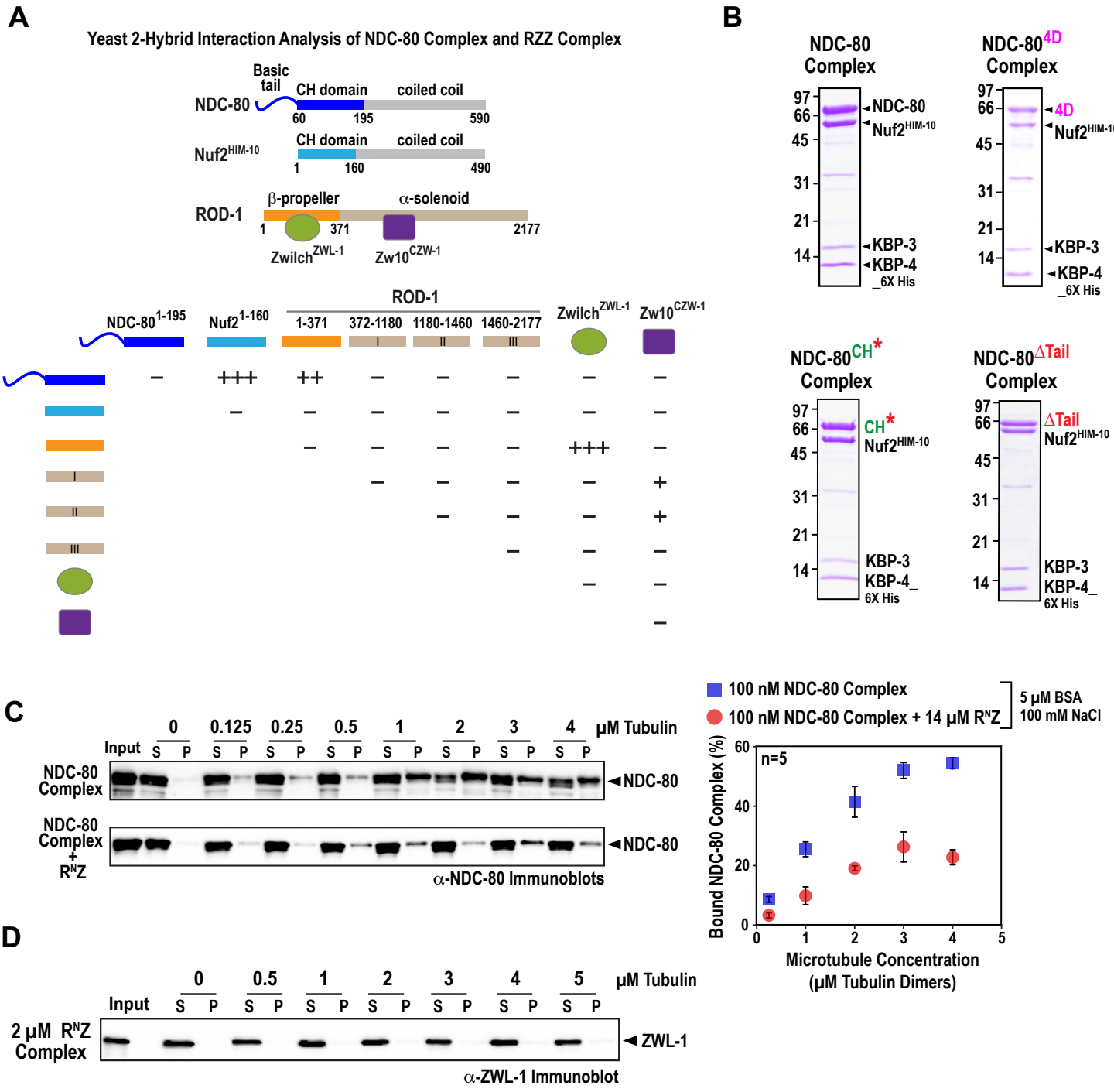

Fig. S2. Yeast two-hybrid and microtubule co-sedimentation analysis.

(A) Schematic of NDC-80, Nuf2^{HIM-10} and RZZ complex subunits and summary of yeast two-hybrid analysis. Strong interaction of Zwilch^{ZWL-1} with the N-terminus of ROD-1, and weak interaction of Zw10^{CZW-1} with internal fragments of ROD-1 indicate that the Zwilch^{ZWL-1} and Zw10^{CZW-1} fusions were expressed in yeast, suggesting that the absence of any interaction between them and the tested NDC-80 and Nuf2^{HIM-10} fragments are not false negatives.

(B) Coomassie-stained gel lanes of recombinant *C. elegans* NDC-80 complexes (WT, ΔTail, 4D or CH*) expressed and purified from bacteria for use in microtubule-binding assays.

(C) Microtubule cosedimentation analysis conducted with indicated concentration of taxol-stabilized microtubules, 100 nM NDC-80 complex, and 14 μM R^{N}Z complex. 5 μM BSA was included in all binding assays conducted in BRB80 buffer supplemented with 100 mM NaCl. Supernatant (S) and Pellet (P) fractions were immunoblotted using anti-NDC-80 antibody. Quantification of the binding analysis is plotted on the right.

(D) Microtubule cosedimentation analysis demonstrating that the R^{N}Z complex does not bind to microtubules. Binding assays were performed with indicated concentrations of taxol-stabilized microtubules, 2 μM R^{N}Z complex, and 5 μM BSA; the binding buffer was BRB80 + 50 mM NaCl. Supernatant (S) and Pellet (P) fractions were immunoblotted using anti-ZWL-1 antibody.

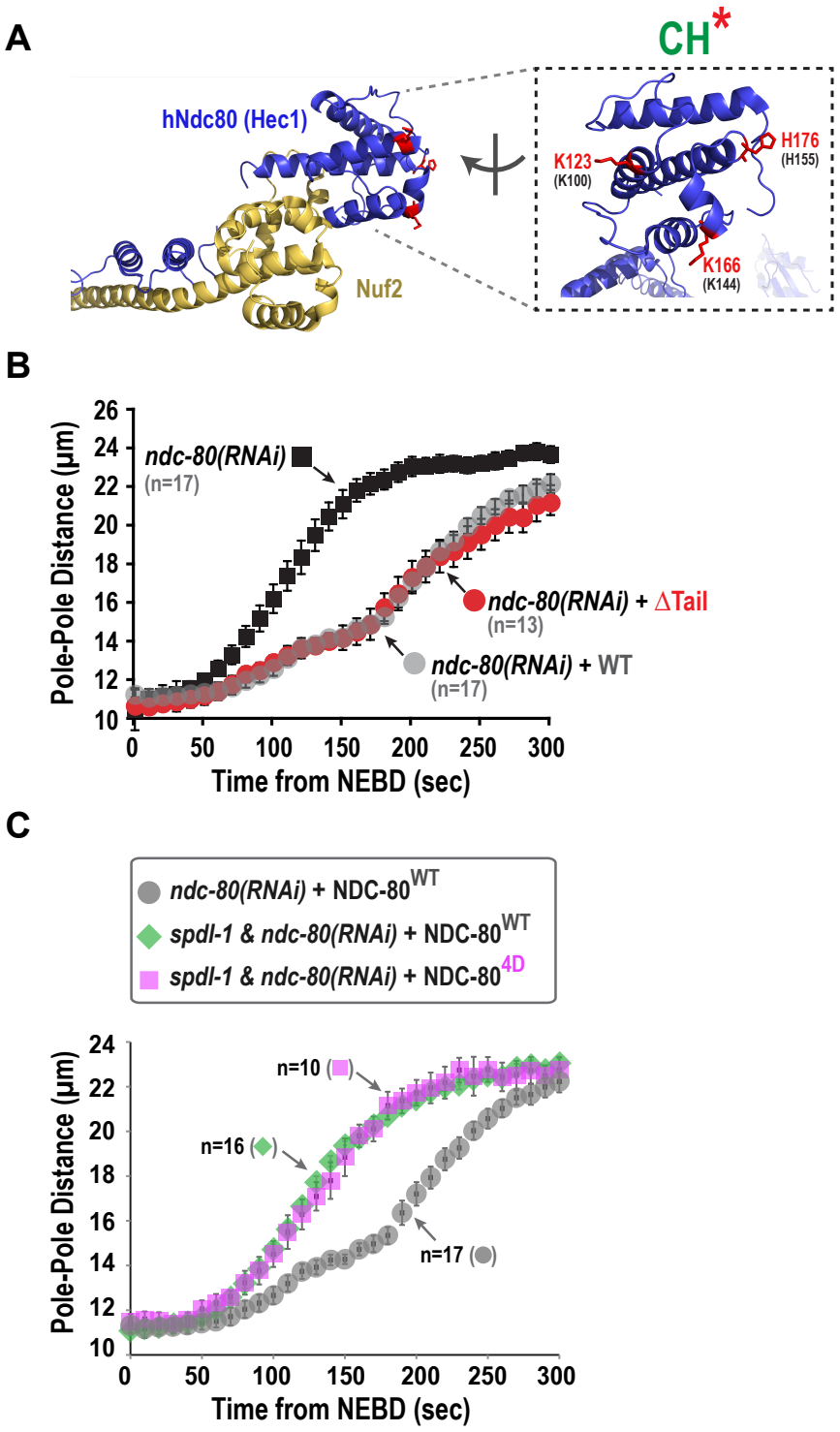

Fig. S3. Location of CH domain mutations, pole separation kinetics of NDC-80$^{\Delta Tail}$, and sensitivity of NDC-80^{4D} to RZZ inhibition.

(A) Location in the structure of the human Ndc80 complex (PDB 2ve7;(15)) of the 3 residues mutated in NDC-80^{CH*}. The red lettering marks the human residues; in parentheses below in black are the corresponding *C. elegans* residues that were mutated to alanine to generate the CH* mutant NDC-80.

(B) Plot of spindle pole separation kinetics, as in *Fig. 1C*. The *ndc-80 (RNAi)* curve is the same as in Fig. 1C and control curve (*ndc-80(RNAi)* + NDC-80^{WT}) is the same as in *Fig. S1F* .

(C) Plot of spindle pole separation kinetics for the indicated conditions. Error bars represent the SEM with a 95% confidence interval. The plot demonstrates that NDC-80^{WT} (*green diamonds*) and NDC-80^{4D} (*pink squares*) are equally sensitive to inhibition by RZZ (induced by depletion of SPDL-1). The control curve (*ndc-80(RNAi)* + NDC-80^{WT}) is the same as in *Fig. S1F*.

Cheerambathur et al. Fig. S4

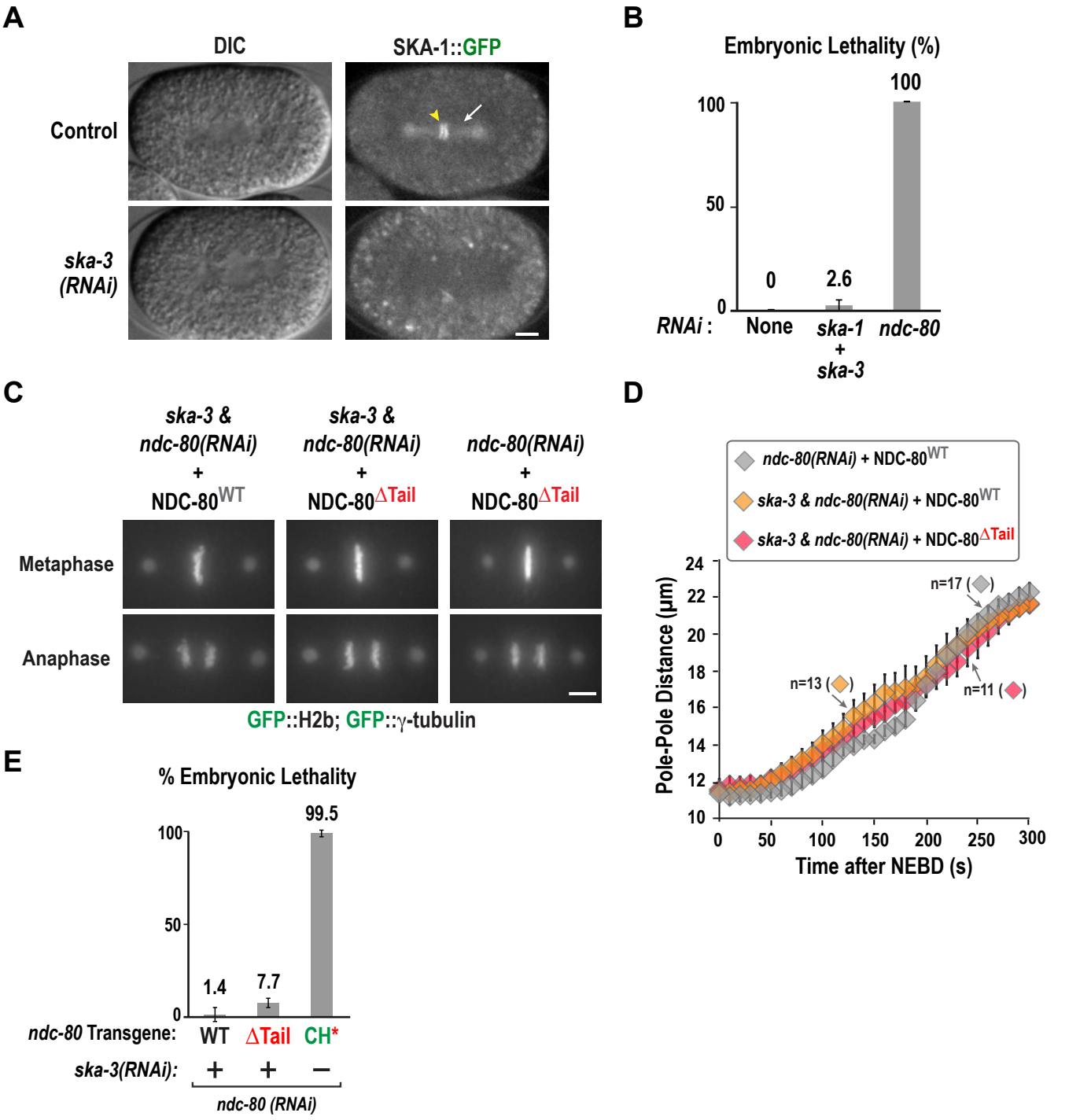

Fig. S4. The Ska complex does not compensate for the absence of the NDC-80 tail.

(A) Evidence that the *ska-3* dsRNA is effective. A strain expressing SKA-1::GFP was imaged at metaphase. In the control metaphase embryo, SKA-1::GFP labels the spindles (*white arrow*) and kinetochores (*yellow arrowhead*) of metaphase embryos. Following SKA-3 depletion, SKA-1::GFP signal is no longer detected (the residual punctate signal is embryo autofluorescence). Bar, 5 µm.

(B) Embryo viability analysis for the indicated conditions. Error bars represent the SD of embryo lethality per worm. >1000 embryos from ≥10 worms were scored per condition. The results show that, in contrast to NDC-80 complex depletion, Ska complex depletion does not lead to significant embryonic lethality.

(C) Chromosome segregation phenotypes for the indicated conditions. Bar, 5 µm.

(D) Plot of spindle pole separation kinetics for the indicated conditions. The *ndc-80(RNAi)* + NDC-80^{WT} curve is the same as in *Fig. S1F*. Error bars represent the SEM with a 95% confidence interval.

(E) Embryo viability analysis for the indicated conditions. Error bars represent the SD of embryo lethality per worm. >1000 embryos from >10 worms were scored for each condition. Depletion of SKA-3 in the presence of ΔTail mutant NDC-80 does not result in embryonic lethality approaching that observed with the CH* mutant NDC-80.

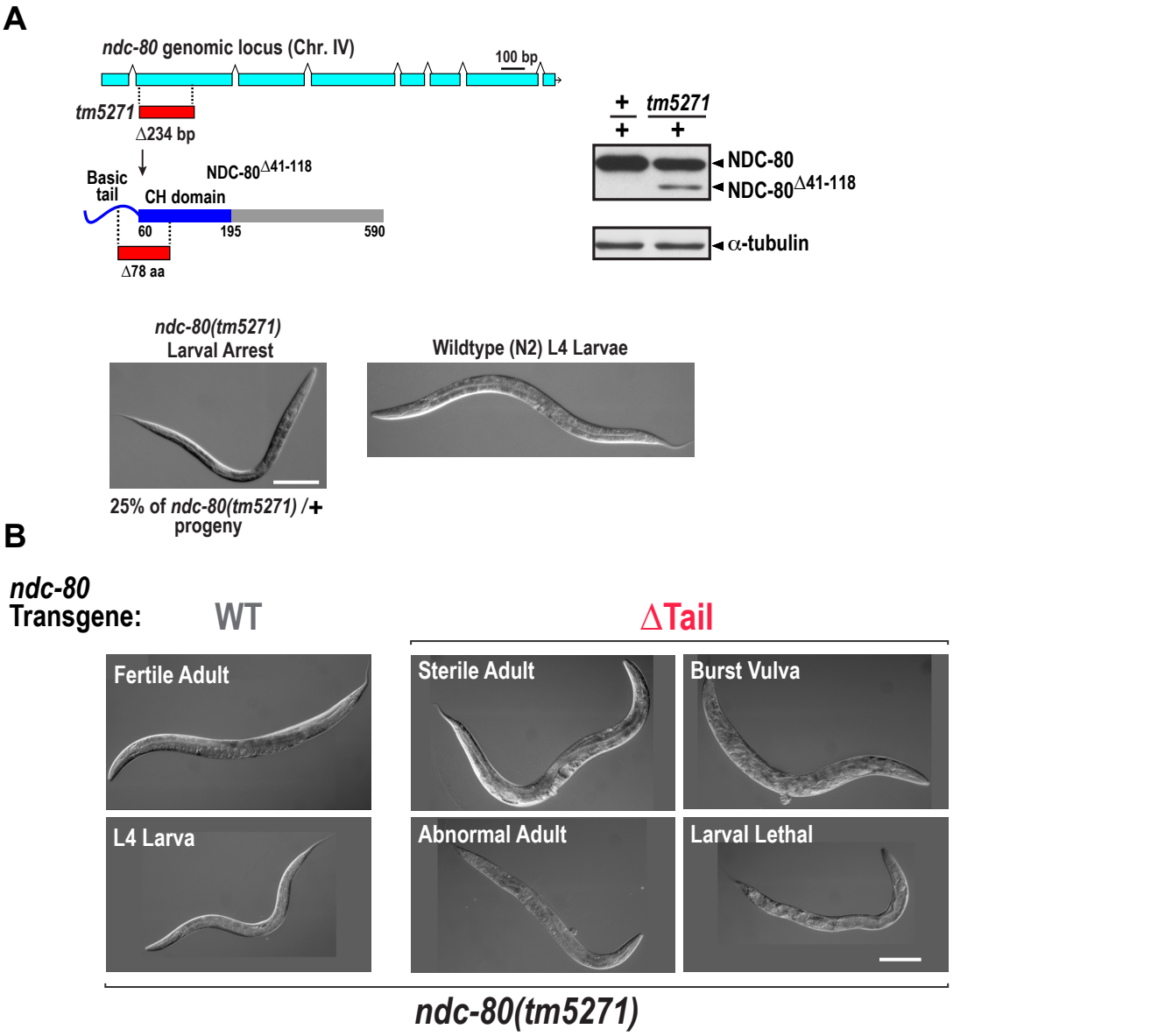

Fig. S5. The *ndc-80(tm5271)* mutant and example phenotypes observed in the presence of *ndc-80*$^{\Delta Tail}$ transgene.

(A) Schematic of the *ndc-80* genomic locus and the *tm5271* deletion mutant allele. The *tm5271* allele is lethal and harbors an in-frame internal deletion, predicted to encode a truncated form of NDC-80 (NDC-80$^{\Delta 41\text{-}118}$), in which part of the basic tail and the initial segment of the NDC-80 CH domain are lacking. In a balanced heterozygous mutant (panel on the right), the predicted truncated NDC-80$^{\Delta 41\text{-}118}$ protein is detectable by immunoblotting. Based on structural and biochemical analysis of the NDC-80 complex (*15, 20*), the in-frame deletion likely abolishes NDC-80 microtubule-binding activity. Homozygous *ndc-80(tm5271)* embryos derived from a heterozygous mother hatch but arrest and die as larvae. As *ndc-80(RNAi)*, which depletes maternal load, causes penetrant embryonic lethality (*Fig. 2E*), the hatching of the mutant embryos is likely supported by maternally loaded wildtype NDC-80 protein. Image panels on the bottom show the larval arrest phenotype compared to a wildtype L4 larva. Bar, 50 µm.

(B) Images of homozygous *ndc-80(tm5271)* worms in the presence of the *ndc-80*^{WT} or *ndc-80*$^{\Delta Tail}$ transgenes. A quantitative description of the phenotypes observed with the *ndc80*$^{\Delta Tail}$ transgene is shown in *Fig. 3D*. Bar, 50 µm.

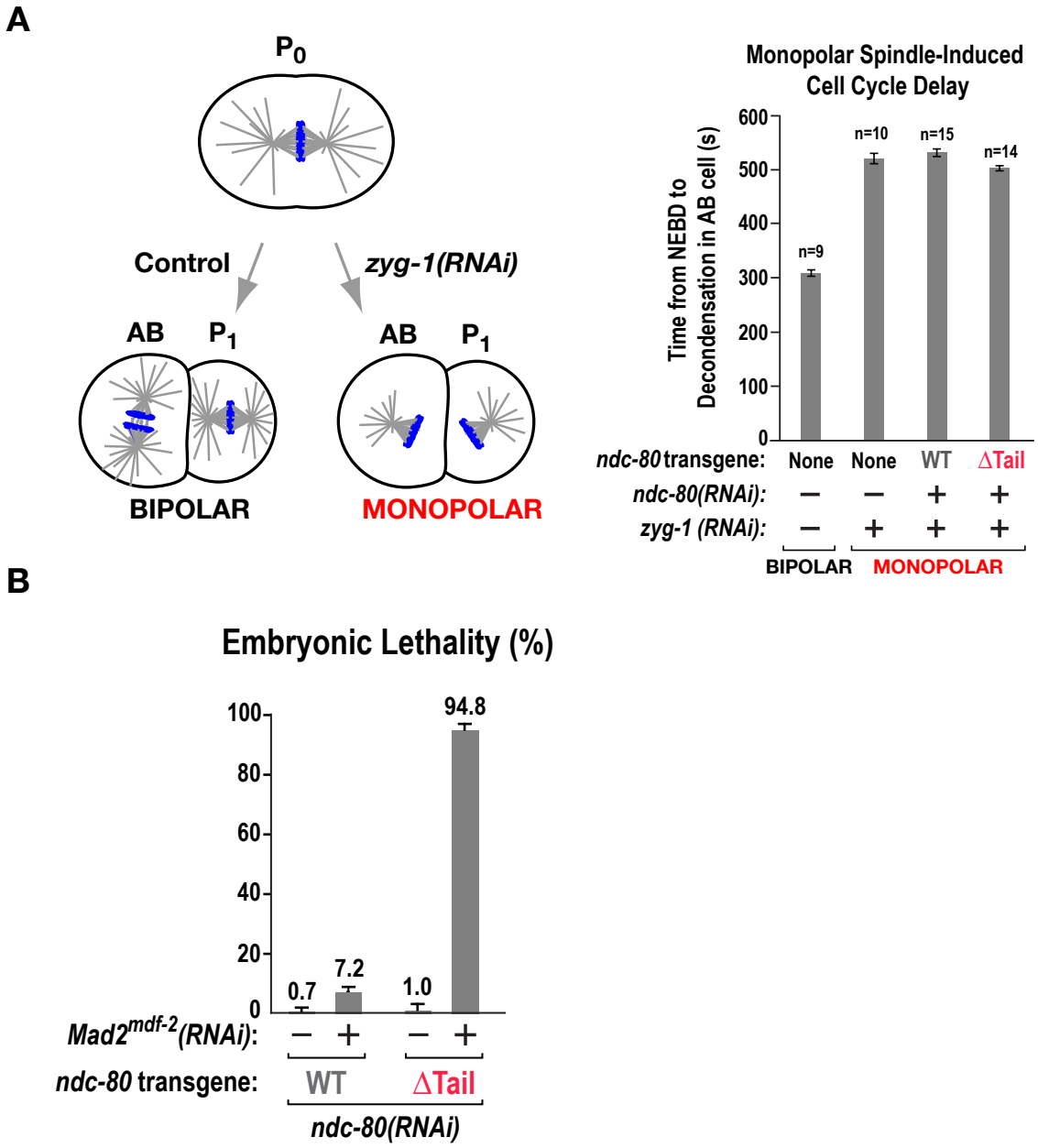

Fig. S6. The spindle checkpoint functions normally in the NDC-80$^{\Delta Tail}$ mutant.

(A) (*left*) Schematic of assay used to generate monopolar versus bipolar second division embryos by depletion of the centriole duplication kinase *zyg-1*. Cell cycle timing is measured in the AB cell in the two types of embryos to assess whether the spindle checkpoint is active (*30*). (*right*) Time from NEBD–Chromosome Decondensation measured in the indicated conditions. Both NDC-80^{WT} and NDC-80$^{\Delta Tail}$ support a monopolar spindle-induced cell cycle delay. By contrast, no delay is observed following NDC-80 depletion (*30*). Error bars represent the SEM with a 95% confidence interval.

(B) Embryo viability analysis for the indicated conditions. Error bars are the SD of embryo lethality per worm; >10 worms and >1000 embryos analyzed per condition.

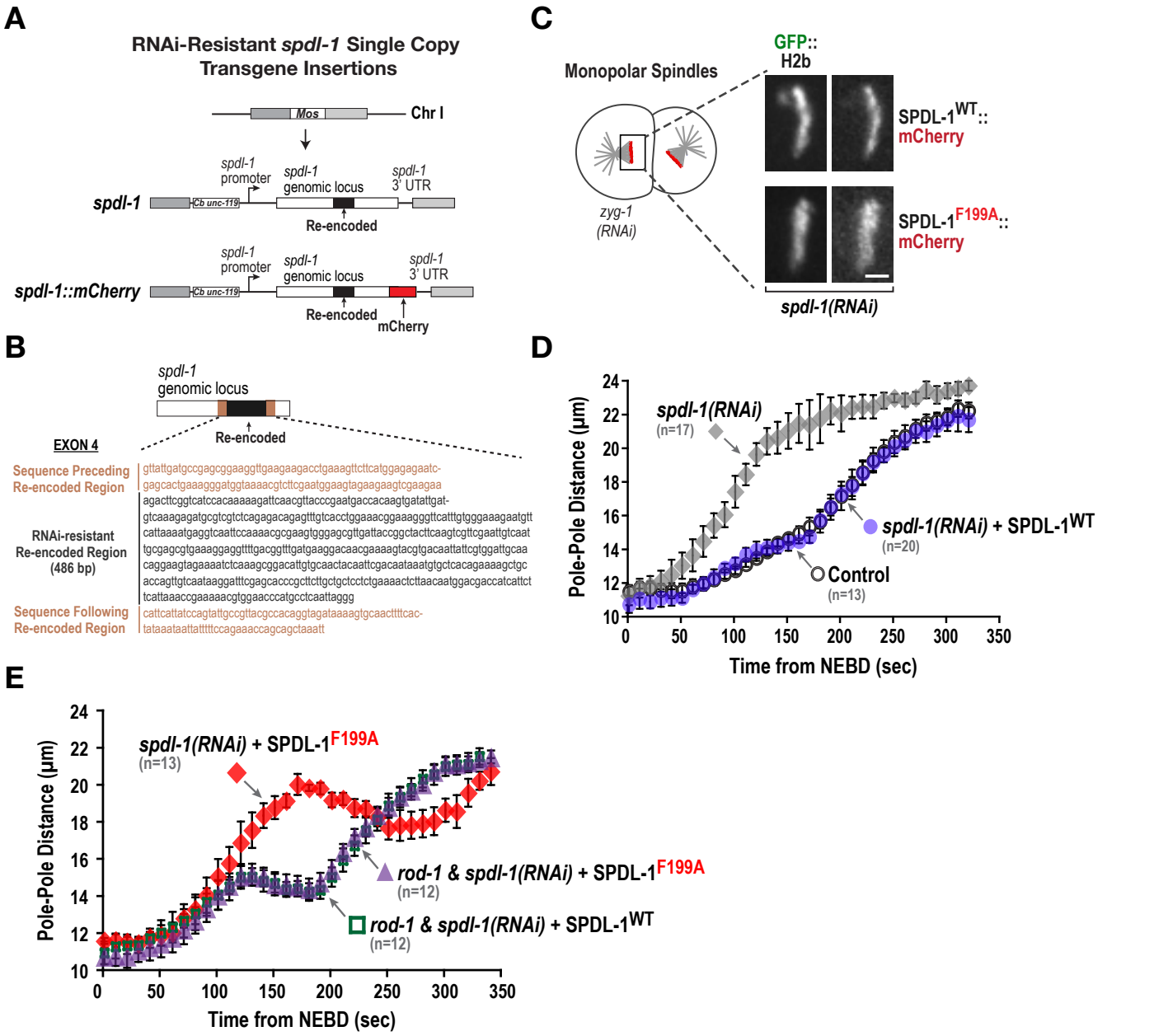

Fig. S7. A replacement system for SPDL-1 in the *C. elegans* embryo.

(A) Schematic of the RNAi-resistant *spdl-1* and *spdl-1::mCherry* transgene integrations (the single Mos transposon used for the integrations was located on Chromosome I for untagged *spdl-1* transgenes and on Chromosome IV for *spdl-1::mCherry* transgenes). The wildtype *spdl-1::mCherry* transgene did not rescue removal of endogenous SPDL-1 as robustly as the untagged *spdl-1* transgene; hence, untagged *spdl-1* transgenes were used for all functional analysis.

(B) Re-encoded nucleotide sequence of exon 4 of *spdl-1* that was used to engineer RNAi-resistance into the *spdl-1* transgene. A dsRNA corresponding to this region was used to deplete endogenous SPDL-1 in all RNAi-based replacement experiments.

(C) Panels showing localization of SPDL-1::mCherry and SPDL-1^{F199A}::mCherry to unattached kinetochores of monopolar spindles generated by depletion of the centriole duplication kinase ZYG-1. Bar, 2.5 µm.

(D) Plot of spindle pole separation kinetics, demonstrating rescue of the defect in formation of kinetochore-microtubule attachments in *spdl-(RNAi)* by the *spdl-1^{WT}* transgene. Error bars represent the SEM with a 95% confidence interval. The control and *spdl-1(RNAi)* curve is the same as in *Fig. 1C*.

(E) Plot of spindle pole separation kinetics, demonstrating the defect in kinetochore-microtubule attachment formation in the presence of SPDL-1^{F199A} (*red diamonds*). Note the perfect overlap between SPDL-1^{WT} (*green outlined squares*) and SPDL-1^{F199A} (*purple triangles*) in the presence of *rod-1(RNAi)*. Error bars represent the SEM with a 95% confidence interval.

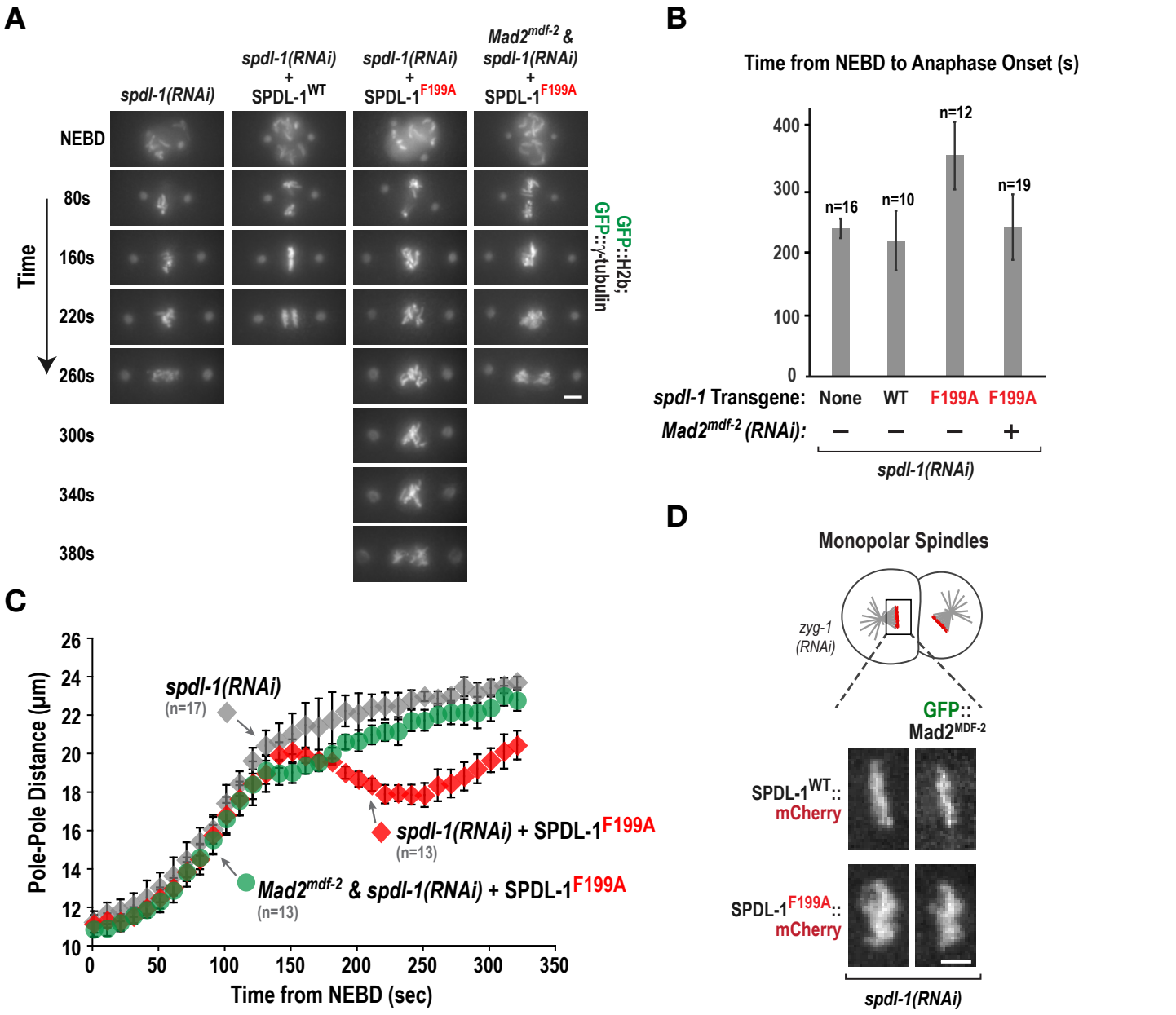

Fig. S8. SPDL-1^{F199A} triggers a spindle checkpoint-dependent cell cycle delay.

In *C. elegans* embryos, SPDL-1 is required for dynein localization to kinetochores (*7*) as well as for spindle checkpoint activation by promoting kinetochore localization of the Mad1/Mad2 complex (*7,31*). This figure shows that SPDL-1^{F199A}, while inhibiting dynein recruitment (*see Fig. 4B*), does not prevent checkpoint activation and in fact triggers a checkpoint-dependent delay. Combining the SPDL-1^{F199A} mutant with checkpoint inhibition (via depletion of the conserved checkpoint protein Mad2^{MDF-2}) recapitulates the SPDL-1 depletion phenotype.

(A) Time-aligned image panels of GFP::H2b and GFP::g-tubulin (relative to NEBD) for the indicated conditions. The images depict delayed anaphase onset in SPDL-1^{F199A} mutant embryos and the abrogation of this delay following spindle checkpoint inhibition by depletion of Mad2^{MDF-2}. Bar, 5µm.

(B) Quantification of the NEBD-anaphase onset interval for the indicated number of embryos per condition. Anaphase onset was defined as the first visible separation of sister chromatids in images of the type shown in panel A. Error bars represent the SD.

(C) Plot of spindle pole separation kinetics, demonstrating that inhibition of the spindle checkpoint in the SPDL-1^{F199A} mutant (*green circles*) results in a profile similar to depletion of SPDL-1 (*gray diamonds*). The *spdl-1(RNAi)* and *spdl-1(RNAi)* + SPDL-1^{F199A} curves are the same as in *Fig.1C* & *S7E*, respectively. Error bars represent the SEM with a 95% confidence interval.

(D) Panels showing recruitment of the spindle checkpoint component Mad2^{MDF-2} to unattached kinetochores of monopolar spindles in SPDL-1::mCherry and SPDL-1^{F199A}::mCherry embryos. Bar, 2.5 µm.

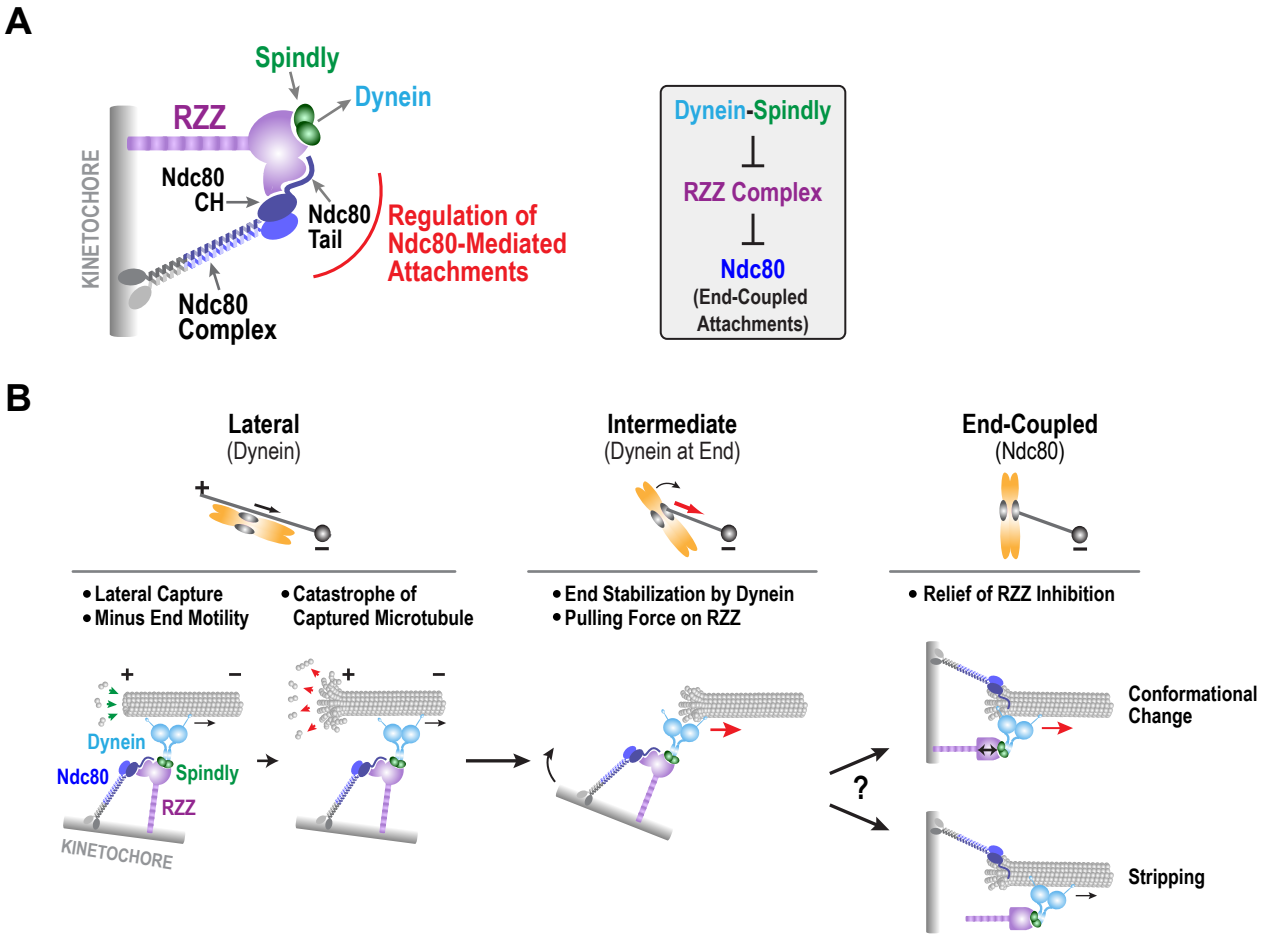

Fig. S9. Model for the transition from dynein-mediated capture to Ndc80-mediated end-coupled attachment.

(A) (*left*) Cartoon summarizing the control of Ndc80 complex microtubule binding by RZZ. As the Ndc80 tail deletion does not exhibit a defect in end-coupled attachment formation in *C. elegans* embryos, we propose that RZZ inhibits Ndc80 via control of the CH domain. (*right*) Dynein recruitment by Spindly is required to turn off RZZ inhibition.

(B) Model, invoking RZZ-mediated inhibition, for the transition from dynein-mediated capture to Ndc80-mediated end-coupled attachment. We propose that it is not solely Spindly-dependent dynein recruitment but rather a subsequent dynein activity-dependent mechanical force that alleviates RZZ inhibition and that this alleviation only occurs when a state that minimizes the potential for merotely is achieved. We postulate that during an initial capture event by kinetochore dynein, RZZ inhibits the Ndc80 complex ("Lateral" state in model). Given the short half-life of mitotic microtubules (*32*), the kinetochore dynein-bound microtubule will catastrophe leading its depolymerizing plus end to reach the kinetochore, where it is stabilized by dynein and exerts a force on the kinetochore dynein module ("Intermediate" state in model)—such a scenario is plausible based on in vitro biophysical experiments analyzing dynein interaction with depolymerizing microtubule ends (*33, 34*). We suggest that this end-coupled force orients the chromosome and alleviates inhibition of Ndc80, either via a change in RZZ conformation or dissociation of RZZ from the kinetochore ("End-coupled" state in model). In this way, RZZ inhibition would help ensure that a kinetochore is oriented toward one spindle pole before end-coupled attachments are formed. Additional mechanisms, including chromokinesins (*35, 36*), likely also contribute to this orientation function.

Supplementary Tables:

Table S1: *C. elegans* strains used in this study

Strain number	Genotype
N2 (ancestral)	
OD927	*unc-119(ed3)III; ltSi421[pDC204;Pspdl-1:spdl-1 reencoded; cb-unc-119(+)]I #1*
OD928	*unc-119(ed3)III; ltSi422[pDC205;Pspdl-1:spdl-1(F199A) reencoded; cb-unc-119(+)]I #1*
OD941	*unc-119(ed3)III; orIs17[dhc-1::dhc-1:GFP;cb-unc- 119(+);ltSi424 spdl-1 [pDC206;Pspdl-1:reencoded; cb-unc-119(+)]II*
OD942	*unc-119(ed3)III; orIs17[dhc-1::dhc-1:GFP;cb-unc-119(+); ltSi425 [pDC205;Pspdl-1:spdl-1(F199A) reencoded; cb-unc-119(+)]I #1*
OD943	*unc-119(ed3)III; ltSi421[pDC207;Pspdl-1:spdl-1reencoded; cb-unc-119(+)]II; ruIs32[pAZ132; pie-1/GFP::histone H2B] III; ddIs6 [GFP::tbg-1; unc-119(+)] V*
OD945	*unc-119(ed3)III; ltSi422[pDC205;Pspdl-1:spdl-1(F199A) reencoded; cb-unc-119(+)]I #1; ruIs32[pAZ132; pie-1/GFP::histone H2B] III; ddIs6 [GFP::tbg-1; unc-119(+)] V*
OD464	*cb-unc-119(+)]IV; ruIs32[pAZ132; pie-1/GFP::histone H2B] III; ddIs6 [GFP::tbg-1; unc-119(+)] V*
OD465	*unc-119(ed3)III; ltSi36[pOD1035/pRG48; Pspdl-1::spdl-1(F199A) reencoded::mCherry; cb-unc-119(+)]IV; ruIs32[pAZ132; pie-1/GFP::histone H2B] III; ddIs6 [GFP::tbg-1; unc-119(+)] V*
OD601	*unc-119(ed3)III; ltSi34[pOD1034/pRG47; Pspdl-1::spdl-1reencoded:: mCherry; cb-unc-119(+)]IV; ltIs52 [pOD379; pie-1/GFP:mdf-2; unc-119 (+)]*
OD602	*unc-119(ed3)III; ltSi36[pOD1035/pRG48; Pspdl-1::spdl-1(F199A) reencoded ::mCherry; cb-unc-119(+)]IV; ltIs52 [pOD379; pie-1/GFP:mdf-2; unc-119 (+)]*
OD611	*unc-119(ed3)III; ltSi425[pDC207;Pspdl-1:SPDL-1(F199A) reencoded; cb-unc-119(+)]II*
OD612	*unc-119(ed3)III; ltSi121[pDC175;Pndc-80:ndc-80 (Mutant D1-59) reencoded; cb-unc-119(+)]II #1*
OD634	*unc-119(ed3)III; ltSi122[pDC178;Pndc-80:ndc-80 (8,18,44,51AAAA) reencoded; cb-unc-119(+)]II #1*
OD642	*unc-119(ed3)III; ltSi129[pDC181;Pndc-80:ndcC-80 (100,144,155AAA) reencoded; cb-unc-119(+)]II #2*
OD613	*unc-119(ed3) III; ltSi120[[pDC170;Pndc-80:ndc-80 reencoded; cb-unc-119(+)]II #3; ruIs32[pAZ132; pie-1/GFP::histone H2B] III; ddIs6 [GFP::tbg-1; unc-119(+)] V*
OD614	*unc-119(ed3) III; ltSi121[pDC175;Pndc-80:ndc-80 (Mutant D1-59) reencoded ; cb-unc-119(+)]II #1; ruIs32[pAZ132; pie-1/GFP::histone H2B] III; ddIs6 [GFP::tbg-1; unc-119(+)] V*
OD644	*unc-119(ed3) III; ltSi122[pDC178;Pndc-80:ndc-80 (8,18,44,51AAAA) reencoded; cb-unc-119(+)]II #1; ruIs32[pAZ132; pie-1/GFP::histone H2B] III; ddIs6 [GFP::tbg-1; unc-119(+)] V*

OD688	*unc-119(ed3) III; ltSi122[pDC178;Pndc-80:ndc-80 (8,18,44,51AAAA) reencoded; cb-unc-119(+)]II #1; ruIs32[pAZ132; pie-1/GFP::histone H2B] III; ddIs6 [GFP::tbg-1; unc-119(+)] V*
OD647	*unc-119(ed3)III; ltSi131[pDC122;Pndc-80:ndc-80:mCherry reencoded; cb-unc-119(+)]II #2; ruIs32[pAZ132; pie-1/GFP::histone H2B] III; ddIs6 [GFP::tbg-1; unc-119(+)] V*
OD1135	*ndc-80(tm5271) IV/nT1[qIs51](IV;V)*
OD1136	*unc-119(ed3)III; ndc-80(tm5271) IV/nT1[qIs51](IV;V);ltSi120[[pDC170;Pndc-80:ndc-80 reencoded; cb-unc-119(+)]II #3ndc-80(tm5271) IV/nT1[qIs51](IV;V)*
OD1137	*unc-119(ed3)III; ndc-80(tm5271) IV/nT1[qIs51](IV;V);ltSi121[pDC175;Pndc-80:ndc-80(D1-59) reencoded; cb-unc-119(+)]II #1ndc-80(tm5271) IV/nT1[qIs51](IV;V)*
OD650	*unc-119(ed3)III; ltSi428[pDC159;Pska-1:ska-1:gfp reencoded; cb-unc-119(+)]II#3*
TH32	*unc-119(ed3) III; ruIs32[pAZ132; pie-1/GFP::histone H2B] III; ddIs6 [GFP::tbg-1; unc-119(+)] V*
OD935	*unc-119(ed3)III; ltSi590[pDC178;Pndc-80:ndc-80 (8,18,44,51DDDD) reencoded; cb-unc-119(+)]II #1*
OD1255	*unc-119(ed3)III; ltSi590[pDC178;Pndc-80:ndc-80 (8,18,44,51DDDD) reencoded; cb-unc-119(+)]II #1; ruIs32[pAZ132; pie-1/GFP::histone H2B] III; ddIs6 [GFP::tbg-1; unc-119(+)] V*

Table S2: Oligos & Templates Used for dsRNA Production

Gene	Oligonucleotide 1	Oligonucleotide 2	Template	mg/mL
W01B6.9 (*ndc-80*)	5'- aattaaccctcactaaagg GATGACAAGTACATT CAGAGATTATACAAAT GATC-3'	5'- taatacgactcactatagg GTGGTTCAAGATTCAT TTGAATATTAAGTCCA CTG-3'	N2 cDNA	2.5
C06A8.5 (*spdl-1*)	5'- aattaaccctcactaaagg AACGTTACCCGAATG ACCAC-3'	5'- taatacgactcactatagg CCTAATTGAGGCATG GGTTC-3'	N2 cDNA	3.7
F55G1.4 (*rod-1*)	5'- aattaaccctcactaaagg AATGCAAATCTTTTTG GATGGGAGAAAC-3'	5'- taatacgactcactatagg CATCGACGAATTTGAT TCGATCAATC-3'	N2 genomic DNA	2.5
Y106G6H.15 (*ska-1*)	5'- aattaaccctcactaaagg TTATGGATAATAGAAA GTCAACG-3'	5'- taatacgactcactatagg ATGGAATCGTTTATTG ATCGGAT-3'	N2 genomic DNA	3.2
F54E7.8 (*ska-3*)	5'- aattaaccctcactaaagg ATGGCTAACGAAACG CTGGAACATG-3'	5'- taatacgactcactatagg AACTCATCAAAAGCCA GTTTTCGTCG-3'	N2 genomic DNA	3.0
Y69A2AR.30 (*mdf-2*)	5'- aattaaccctcactaaagg GTGAACTGACGTCGA GAATGAG-3'	5'- taatacgactcactatagg GACGGATGTAAAGAC ACAAAACG-3'	N2 genomic DNA	4.4
F59E12.2 (*zyg-1*)	5'- aattaaccctcactaaagg GGACGGAAATTCAAA CGAT-3'	5'- taatacgactcactatagg AACGAAATTCCCTTGA GCTG-3'	N2 genomic DNA	4.0

* Lowercase letters denote T3 and T7 sequences included for RNA synthesis.

References:

1. I. M. Cheeseman, A. Desai, Molecular architecture of the kinetochore-microtubule interface, *Nat. Rev. Mol. Cell Biol.* **9**, 33–46 (2008).

2. S. Santaguida, A. Musacchio, The life and miracles of kinetochores, *EMBO J.* **28**, 2511–2531 (2009).

3. C. L. Rieder, S. P. Alexander, Kinetochores are transported poleward along a single astral microtubule during chromosome attachment to the spindle in newt lung cells, *J. Cell Biol.* **110**, 81–95 (1990).

4. C. L. Rieder, E. D. Salmon, The vertebrate cell kinetochore and its roles during mitosis, *Trends Cell Biol.* **8**, 310–318 (1998).

5. F. Scaërou *et al.*, The rough deal protein is a new kinetochore component required for accurate chromosome segregation in Drosophila, *J. Cell. Sci.* **112 (Pt 21)**, 3757–3768 (1999).

6. D. A. Starr, B. C. Williams, T. S. Hays, M. L. Goldberg, ZW10 helps recruit dynactin and dynein to the kinetochore, *J. Cell Biol.* **142**, 763–774 (1998).

7. R. Gassmann *et al.*, A new mechanism controlling kinetochore-microtubule interactions revealed by comparison of two dynein-targeting components: SPDL-1 and the Rod/Zwilch/Zw10 complex, *Genes Dev.* **22**, 2385–2399 (2008).

8. R. Karess, Rod-Zw10-Zwilch: a key player in the spindle checkpoint, *Trends Cell Biol.* **15**, 386–392 (2005).

9. E. R. Griffis, N. Stuurman, R. D. Vale, Spindly, a novel protein essential for silencing the spindle assembly checkpoint, recruits dynein to the kinetochore, *J. Cell Biol.* **177**, 1005–1015 (2007).

10. K. Oegema, A. Desai, S. Rybina, M. Kirkham, A. A. Hyman, Functional analysis of kinetochore assembly in Caenorhabditis elegans, *J. Cell Biol.* **153**, 1209–1226 (2001).

11. A. Desai *et al.*, KNL-1 directs assembly of the microtubule-binding interface of the kinetochore in C. elegans, *Genes Dev.* **17**, 2421–2435 (2003).

12. M. Barisic *et al.*, Spindly/CCDC99 is required for efficient chromosome congression and mitotic checkpoint regulation, *Mol. Biol. Cell* **21**, 1968–1981 (2010).

13. I. M. Cheeseman, J. S. Chappie, E. M. Wilson-Kubalek, A. Desai, The conserved KMN network constitutes the core microtubule-binding site of the kinetochore, *Cell* **127**, 983–997 (2006).

14. J. G. Deluca *et al.*, Kinetochore microtubule dynamics and attachment stability are regulated by Hec1, *Cell* **127**, 969–982 (2006).

15. C. Ciferri *et al.*, Implications for kinetochore-microtubule attachment from the structure

of an engineered Ndc80 complex, *Cell* **133**, 427–439 (2008).

16. F. Civril *et al.*, Structural analysis of the RZZ complex reveals common ancestry with multisubunit vesicle tethering machinery, *Structure* **18**, 616–626 (2010).

17. G. J. Guimaraes, Y. Dong, B. F. McEwen, J. G. Deluca, Kinetochore-microtubule attachment relies on the disordered N-terminal tail domain of Hec1, *Curr. Biol.* **18**, 1778–1784 (2008).

18. S. A. Miller, M. L. Johnson, P. T. Stukenberg, Kinetochore attachments require an interaction between unstructured tails on microtubules and Ndc80(Hec1), *Curr. Biol.* **18**, 1785–1791 (2008).

19. N. T. Umbreit *et al.*, The Ndc80 kinetochore complex directly modulates microtubule dynamics, *Proc. Natl. Acad. Sci. U.S.A.* **109**, 16113–16118 (2012).

20. G. M. Alushin *et al.*, The Ndc80 kinetochore complex forms oligomeric arrays along microtubules, *Nature* **467**, 805–810 (2010).

21. R. R. Wei, J. Al-Bassam, S. C. Harrison, The Ndc80/HEC1 complex is a contact point for kinetochore-microtubule attachment, *Nat. Struct. Mol. Biol.* **14**, 54–59 (2007).

22. F. Lampert, C. Mieck, G. M. Alushin, E. Nogales, S. Westermann, Molecular requirements for the formation of a kinetochore-microtubule interface by Dam1 and Ndc80 complexes, *J. Cell Biol.* (2012), doi:10.1083/jcb.201210091.

23. J. P. I. Welburn *et al.*, Aurora B phosphorylates spatially distinct targets to differentially regulate the kinetochore-microtubule interface, *Mol. Cell* **38**, 383–392 (2010).

24. J. C. Schmidt *et al.*, The kinetochore-bound ska1 complex tracks depolymerizing microtubules and binds to curved protofilaments, *Dev. Cell* **23**, 968–980 (2012).

25. K. K. Stein, E. S. Davis, T. Hays, A. Golden, Components of the spindle assembly checkpoint regulate the anaphase-promoting complex during meiosis in Caenorhabditis elegans, *Genetics* **175**, 107–123 (2007).

26. R. Gassmann *et al.*, Removal of Spindly from microtubule-attached kinetochores controls spindle checkpoint silencing in human cells, *Genes Dev.* **24**, 957–971 (2010).

27. D. Cimini *et al.*, Merotelic kinetochore orientation is a major mechanism of aneuploidy in mitotic mammalian tissue cells, *J. Cell Biol.* **153**, 517–527 (2001).

28. C. Frøkjaer-Jensen *et al.*, Single-copy insertion of transgenes in Caenorhabditis elegans, *Nat. Genet.* **40**, 1375–1383 (2008).

29. S. Tan, A modular polycistronic expression system for overexpressing protein complexes in Escherichia coli, *Protein Expr. Purif.* **21**, 224–234 (2001).

30. A. Essex, A. Dammermann, L. Lewellyn, K. Oegema, A. Desai, Systematic analysis in Caenorhabditis elegans reveals that the spindle checkpoint is composed of two largely

independent branches, *Mol. Biol. Cell* **20**, 1252–1267 (2009).

31. T. G. Yamamoto, S. Watanabe, A. Essex, R. Kitagawa, SPDL-1 functions as a kinetochore receptor for MDF-1 in Caenorhabditis elegans, *J. Cell Biol.* **183**, 187–194 (2008).

32. E. D. Salmon, R. J. Leslie, W. M. Saxton, M. L. Karow, J. R. McIntosh, Spindle microtubule dynamics in sea urchin embryos: analysis using a fluorescein-labeled tubulin and measurements of fluorescence redistribution after laser photobleaching, *J. Cell Biol.* **99**, 2165–2174 (1984).

33. L. Laan *et al.*, Cortical dynein controls microtubule dynamics to generate pulling forces that position microtubule asters, *Cell* **148**, 502–514 (2012).

34. A. G. Hendricks *et al.*, Dynein tethers and stabilizes dynamic microtubule plus ends, *Curr. Biol.* **22**, 632–637 (2012).

35. J. Powers *et al.*, Loss of KLP-19 polar ejection force causes misorientation and missegregation of holocentric chromosomes, *J. Cell Biol.* **166**, 991–1001 (2004).

36. V. Magidson *et al.*, The spatial arrangement of chromosomes during prometaphase facilitates spindle assembly, *Cell* **146**, 555–567 (2011).